Mechanism of cyclic β-glucan export by ABC transporter Cgt of *Brucella*

Jaroslaw Sedzicki[1*], Dongchun Ni[2*], Frank Lehmann[1], Na Wu[3], Renato Zenobi[3], Seunho Jung[4], Henning Stahlberg[2#] and Christoph Dehio[1#]

[1]Biozentrum, University of Basel, Basel, Switzerland

[2]Laboratory of Biological Electron Microscopy (LBEM), IPHYS, SB, EPFL, and Dept. of Fundamental Microbiology, Faculty of Biology and Medicine, University of Lausanne, Switzerland

[3]Dept. of Chemistry and Applied Biosciences, ETH Zürich, Zürich, Switzerland

[4]Dept. of Systems Biotechnology & Dept. of Bioscience and Biotechnology, Konkuk University, Seoul, Korea

[*]These authors contributed equally to this work

[#]Corresponding authors: Christoph Dehio (christoph.dehio@unibas.ch); Henning Stahlberg (henning.stahlberg@epfl.ch)

Abstract

Polysaccharides play critical roles in bacteria, including the formation of protective capsules and biofilms and for establishing specific host cell interactions. Their transport across membranes is often mediated by ABC transporters, which utilize ATP to translocate diverse molecules. Cyclic β-glucans (CβGs) are critical for host interaction of the *Rhizobiales*, including the zoonotic pathogen *Brucella*. CβGs are exported into the periplasmic space by the cyclic glucan transporter (Cgt). The interaction of an ABC transporter with a polysaccharide substrate has not been visualized so far. Here we use single-particle cryo-electron microscopy (cryo-EM) to elucidate the structures of Cgt from *Brucella abortus* in four conformational states. The substrate-bound structure reveals an unusual binding pocket at the height of the cytoplasmic leaflet, while ADP-vanadate models hint to an alternative mechanism of substrate release. Our work provides insights into the translocation of large, heterogenous substrates and sheds light on protein-polysaccharide interactions in general.

Introduction

With over 500,000 new cases reported every year, brucellosis is the most common bacterial zoonosis. This debilitating illness can lead to many health consequences, often requires prolonged antibiotic treatment and has a high relapse potential. In addition, animal brucellosis disrupts livestock production, resulting in significant losses in agriculture[1,2].

Successful infection of the host by *Brucella* requires the establishment of an intracellular replicative niche inside of the host endoplasmic reticulum[3]. This complex interaction with the host cell is driven by virulence factors, including the type IV secretion system, modified LPS and CβGs[4-6].

In *Brucella,* CβG synthesis is orchestrated by three membrane proteins (Fig. 1a). The main cyclic glucan chain is synthesized in the cytoplasm by the cyclic glucan synthase (Cgs), and exported to the periplasmic space by Cgt, a predicted type IV ABC exporter[7]. Finally, cyclic glucan modifier (Cgm) adds negatively charged succinate side chains, resulting in an anionic character of CβG. Deletion mutants of *cgs* or *cgt* are strongly attenuated in both *in vitro* and *in vivo* infection models[5]. Studies of the CβG synthesis pathway can potentially provide new strategies of combating brucellosis.

CβGs are cyclic polymers of D-glucose linked uniformly by β-1,2-glycosidic bonds. The number of glucose molecules in the glucan chain (Degree of Polymerization, DP) varies and CβGs produced by a given species represent a mixture of molecular sizes. Typically, the DP value is within the range from 17 to 25[6].

Despite the importance of ABC transporters in polysaccharide secretion[7,8], no structures visualizing substrate interaction are available to date. The mechanism underlying the interaction of Cgt with its complex glucan substrate leaves many unresolved questions. Cgt needs to specifically recognize the β-1,2-glucan backbone while retaining a high level of tolerance for the heterogeneous substrate size. This makes Cgt a potential source of new

insights into translocation of large substrates by ABC transporters as well as protein-carbohydrate interactions in general.

Here, we used cryo-EM to characterize Cgt from *Brucella abortus* (*Bab*) in different conformations. We report a structure of an ABC transporter bound to a polysaccharide cargo as well as a modified outward-facing conformation. In addition, we provide functional data that complement our structure observations. Taken together, our work elucidates a number of aspects of the transporting cycle of Cgt, with insights into the specific structural features that allow the recognition, binding and release of its large, size-variable glucan substrate.

Results

Role of Cgt in the CβG pathway. In order to study the functional aspects of *B. abortus* Cgt, we used the related plant pathogen *A. tumefaciens* strain C58 (*Atu*) as a model organism. CβGs are essential for the adaptation of *Atu* to low osmotic pressure[9]. To confirm the role of ABC transporter activity of *Bab* Cgt in CβG export, we generated a *cgt* deletion mutant of *Atu* (*Atu* Δ*cgt*) and checked if the gene encoding the *Bab* homolog rescues growth in the low osmolarity medium YPL (Fig. 1b, Extended Data Fig. 1a). While *Atu Δcgt* was unable to grow in YPL, growth was restored by introducing a plasmid encoding for wild type *Bab cgt* (cgt_{WT}). The Walker B cgt_{E497Q} mutant failed to restore growth. The addition of 100 mM NaCl to YPL restored growth in all conditions, indicating that the observed phenotypes depend on low osmolarity. These results indicate that CβG export is linked to Cgt ABC transporter activity.

***In vitro* substrate interactions.** We then looked closer at the interactions of purified Cgt with its natural substrate. We were able to successfully express the protein in *E. coli* and reconstitute it in lipid nanodiscs[10] (Extended Data Fig. 2). As for the substrate, we used CβGs purified to homogeneity from *R. leguminosarum* (*Rle*). *Rle* glucans have a DP of 17-25, similar to the size distribution found in both *Brucella* and *Agrobacterium*. In addition, *Rle* glucans are mostly

unsubstituted, which makes them similar to newly synthesized neutral CβGs in *Brucella* cytoplasm[6,11].

We assessed the influence of the substrate on the ATPase activity of Cgt using the malachite green assay (Fig. 1c). The activity of some ABC transporters is stimulated in the presence of their substrates. Interestingly, we observed a decrease of Cgt ATPase rate upon the addition of CβG. It has been recently proposed that particularly large substrates can slow down the kinetics of ABC transporters, as in the case of 18-meric peptide transport by TAPL[12]. We propose that CβGs, with molecular weight in the range of 3 kDa, may represent a similar kinetic of substrate interaction. Cgt_{E497Q} mutant displayed background-level activity.

Since natural CβGs constitute a mixture of sugar sizes, we wanted to determine if Cgt has a preference *in vitro* for a certain glucan subpopulation. To this end, Cgt was incubated with purified *Rle* CβGs, followed by extensive buffer exchange in order to remove excess glucan. The resulting samples were subjected to mass spectroscopy (MS) (Fig. 1d). The analysis indicated that purified Cgt has a strong preference for small glucan rings (DP=17-18) that correspond to the lower end of the size distribution found *in vivo* for both *R. leguminosarum* and *B. abortus*, where the main species has a DP of 19[6,11]. No molecular species within this size range were observed in the glucan-free sample, indicating that no large polysaccharide chains were carried over from the *E. coli* expression strain.

In order to determine if Cgt alone is sufficient to translocate the substrate across lipid bilayers, we developed a proteoliposome (PLS) assay for glucan translocation (Fig. 1e, Extended Data Fig. 2d, e). Purified Cgt was reconstituted into liposomes and their ability to uptake CβG was assessed by MS analysis of the proteoliposome fraction. The results indicated that Cgt can translocate CβGs across membranes in an ATP-dependent manner. We observed the uptake of mostly small glucan chains, confirming that the substrate size preference is not induced by the presence of the nanodisc.

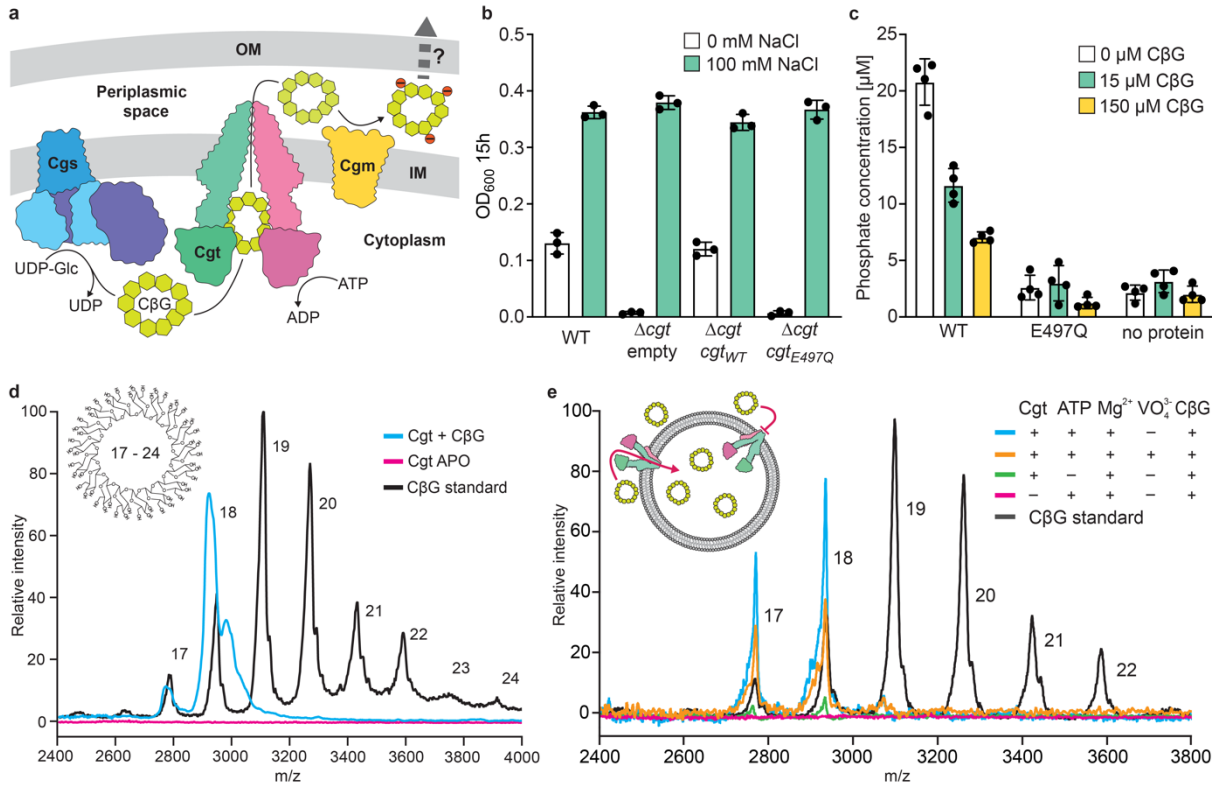

Fig. 1 | Function of Cgt. a, CβG synthesis pathway. Cgs is responsible for the generation of the main glucan backbone, which is exported across the inner membrane (IM) by Cgt. In the periplasm, the Cgm adds negatively charged side chains to the glucan. **b**, Catalytically active Cgt is required for adaptation of *A. tumefaciens* to low osmotic pressure. OD_{600} values at 15 h time point in YPL medium (white) or YPL supplemented with 100 mM NaCl (green). The *Atu Δcgt* mutant can be rescued with WT *B. abortus cgt* gene, but not with the Walker B cgt_{E497Q} mutant. Addition of 100 mM NaCl restored growth of all strains. Dots represent mean values of independent experiments (n=3). Error bars represent standard deviation. **c**, Malachite green ATPase assay with nanodisc-reconstituted Cgt. Cgt WT shows substantial basal activity, which is inhibited by increasing concentrations of substrate. The E497Q mutant displays background ATPase activity. Dots represent mean values of independent experiments (n=4). Error bars represent standard deviation. **d**, MALDI-TOF analysis of CβG binding. Following incubation with substrate and buffer exchange, 17- and 18-meric CβGs remain associated with Cgt (blue). Higher molecular weight glucans present in the initial CβG sample (black) do not associate with the protein. **e**, MALDI-TOF analysis of CβG uptake into Cgt proteoliposomes. Similar preference of the transporter for 17- and 18-meric CβGs was observed.

Cgt structure determination. We then set out to characterize Cgt structurally using cryo-electron microscopy (cryo-EM). We used different approaches of sample preparation in an attempt to capture different transporter conformations. We were able to generate four distinct models of Cgt (Fig. 2a-d). Three were obtained using nanodisc-reconstituted protein and were sufficient for model building: substrate-free Cgt_{E497Q} (Cgt_{APO}), Cgt_{E497Q} bound to CβG (Cgt_{SUB})

and Cgt_{WT} bound to ADP-orthovanadate (Cgt_{VAN}). The fourth structure (Cgt_{DET}) was generated using a lower resolution map obtained with a LMNG-reconstituted, ADP-orthovanadate-bound protein (for details concerning image processing and resulting maps see Extended Data Fig. 3-6).

Our structures reveal a homodimer of Cgt that assumes a type IV ABC exporter fold, similar to bacterial MsbA as well as human ABCB1 (Fig. 2a, b, Supp. Video 1). Each monomer is composed of 6 transmembrane helices (TM1-6), followed by a nucleotide-binding domain (NBD). TM helices 4 and 5 are 'swapped' between Cgt monomers and can undergo large rearrangements. This results in a hinge movement that allows changes in the distance between the NBDs from both monomers (Extended data Fig. 7a). In the Cgt_{APO} and Cgt_{SUB} structures, the NBDs are positioned relatively far away from each other, resulting in a large central cavity opened to the cytosolic side. The volume of the cavity is additionally expanded by the unusual curvature of TM5 that is facilitated by residues P234 and G244 (Fig. 2f, Extended Data Fig. 7b, c).

Substrate-bound model of Cgt. The Cgt_{SUB} map allowed the docking of a complete 18-meric CβG chain into the Cgt model. The glucan is spread between both monomers of Cgt and binds to symmetric pockets at the border of the inner membrane leaflet (Fig. 3a, b, Extended data Fig. 7d-f). Each of the binding pockets is formed by TM helices 2 and 3 of one monomer and TMs 4 and 5 of the other, with the kink of TM5 forming the inner limit. The docking of the CβG requires an extended, flattened conformation of the glucan chain that is distinct from the condensed shape predicted for the solution state[13]. Substrate binding leads to rearrangements of TM helices involved in substrate binding; however no major shifts are observed (Fig. 3c, Supp. Video 2). The curvature of the TM5 appears to be one of the elements defining the geometry of the substrate binding pocket.

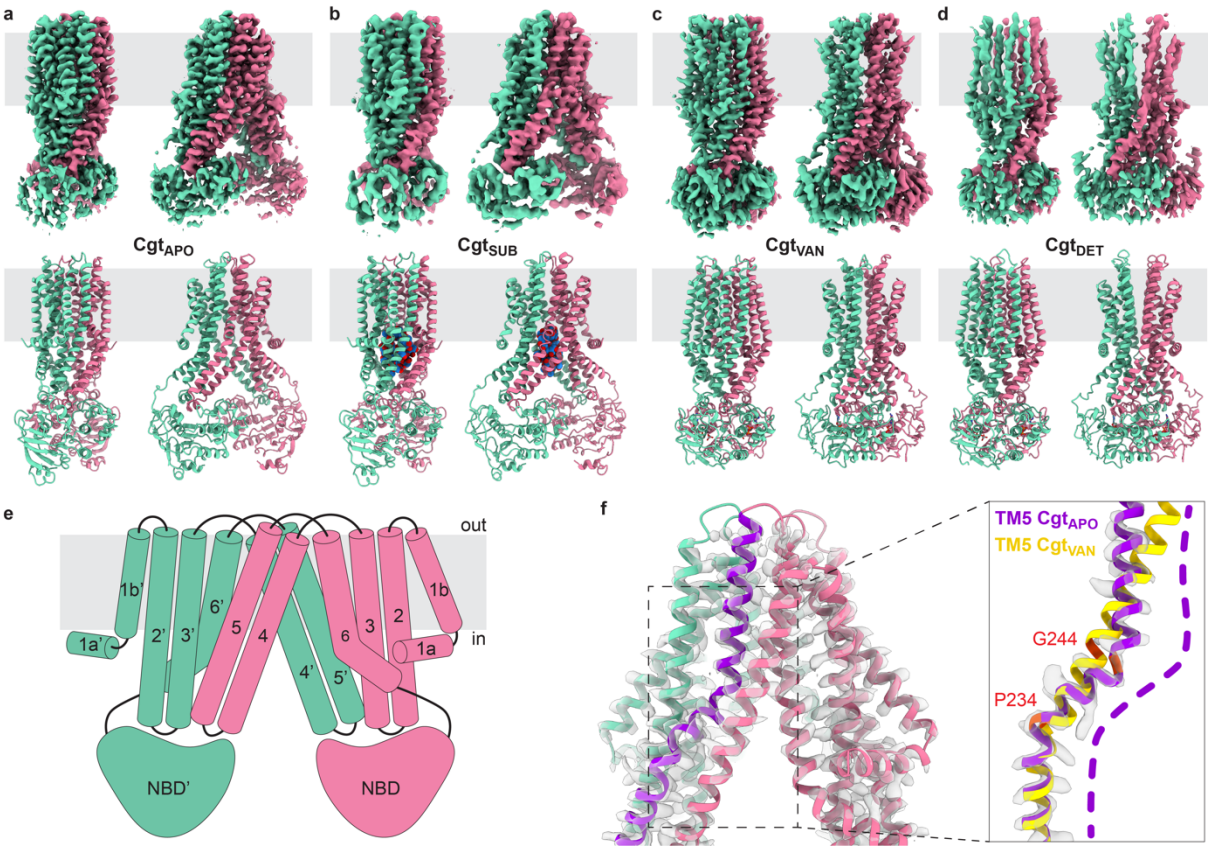

Fig. 2 | Structural models of Cgt. **a-d**, Cryo-EM density maps (top) and corresponding models (bottom) of *B. abortus* Cgt generated in this study. Pink, chain A; green, chain B; blue-red spheres, CβG. Membrane boundaries are indicated with gray. **e**, Cartoon depicting the topology of Cgt, with numbered transmembrane helices. NBD, nucleotide binding domain. **f**, Cgt_{APO} structure and the corresponding density map with TM5 highlighted in purple. Close-up shows an overlay of TM5 of Cgt_{APO} (purple) and Cgt_{VAN} (yellow) models showing the strong curvature of the helix in the inward-facing state (illustrated by dashed line). Cryo-EM density of Cgt_{APO} is shown. Residues P234 and G244 contributing to the curvature of TM5 are shown in red. Contour levels are 0.8 (a), 0.55 (b), 0.7 (c), 0.45 (d), 1.9 (f).

Only 5-6 glucose subunits of the CβG chain are directly engaged within each of the symmetric binding pockets. The experimental densities corresponding to these parts of the glucan are well defined, suggesting specific interactions with Cgt. The remaining parts of the glucan span across the center of the inner cavity and do not interact directly with the protein. The weaker experimental densities corresponding to these parts of the substrate suggest increased flexibility (Fig. 3d, Supp. Video 3). We propose that *in vivo* this flexibility allows the packing of glucan chains of varying length.

In order to verify the relevance of the binding pocket residues in CβG docking, we performed a screen in which we tested the ability of point mutants of *Bab cgt* to restore growth

of *Atu Δcgt* under different levels of osmotic stress (Fig. 3e; Extended Data Fig. 1b-e). The results indicate that substrate interaction is mediated by two groups of polar and charged residues: E188/H191/Q232 of TMs 4 and 5 of one Cgt monomer and D81/H85/R121/D124/R135 form TMs 2 and 3 of the other (Supp. Video 4). In addition, two aromatic residues are located at the borders of the interface: W239 at the inner and F195 at the outer limit. Mutations of residues D81/R121/E188/Q232/W239 showed clear phenotypes even in the presence of 15 mM NaCl, suggesting their critical role.

Compared to the lipid A core binding position in MsbA[7], CβG is docked much closer to the outside limits of the central cavity, leaving a large, inner area of the cavity unoccupied (Extended Data Fig. 7f). At its inner limit, the central cavity of both inward-facing conformations is separated from the periplasmic space by a hydrophobic 'isoleucine gate' formed residues I46 and I276 (Extended Data Fig. 8a).

Nucleotide-bound structures. In contrast to nucleotide-free models, the NBDs of the Cgt_{VAN} and Cgt_{DET} structures are locked in a dimeric, post-hydrolysis state (Fig. 4, Supp. Video 5), separating the central cavity from the cytosol. In the Cgt_{VAN} structure, the central cavity is closed from both sides, indicating an occluded conformation previously reported for other ABC exporters (Extended Data Fig. 8b)[7]. Densities corresponding to ADP and the orthovanadate ion at the NBD dimer interface were present in our experimental map (Fig. 4a). We did not observe a density corresponding to the Mg^{2+} ion, implying that it has been already released following ATP hydrolysis.

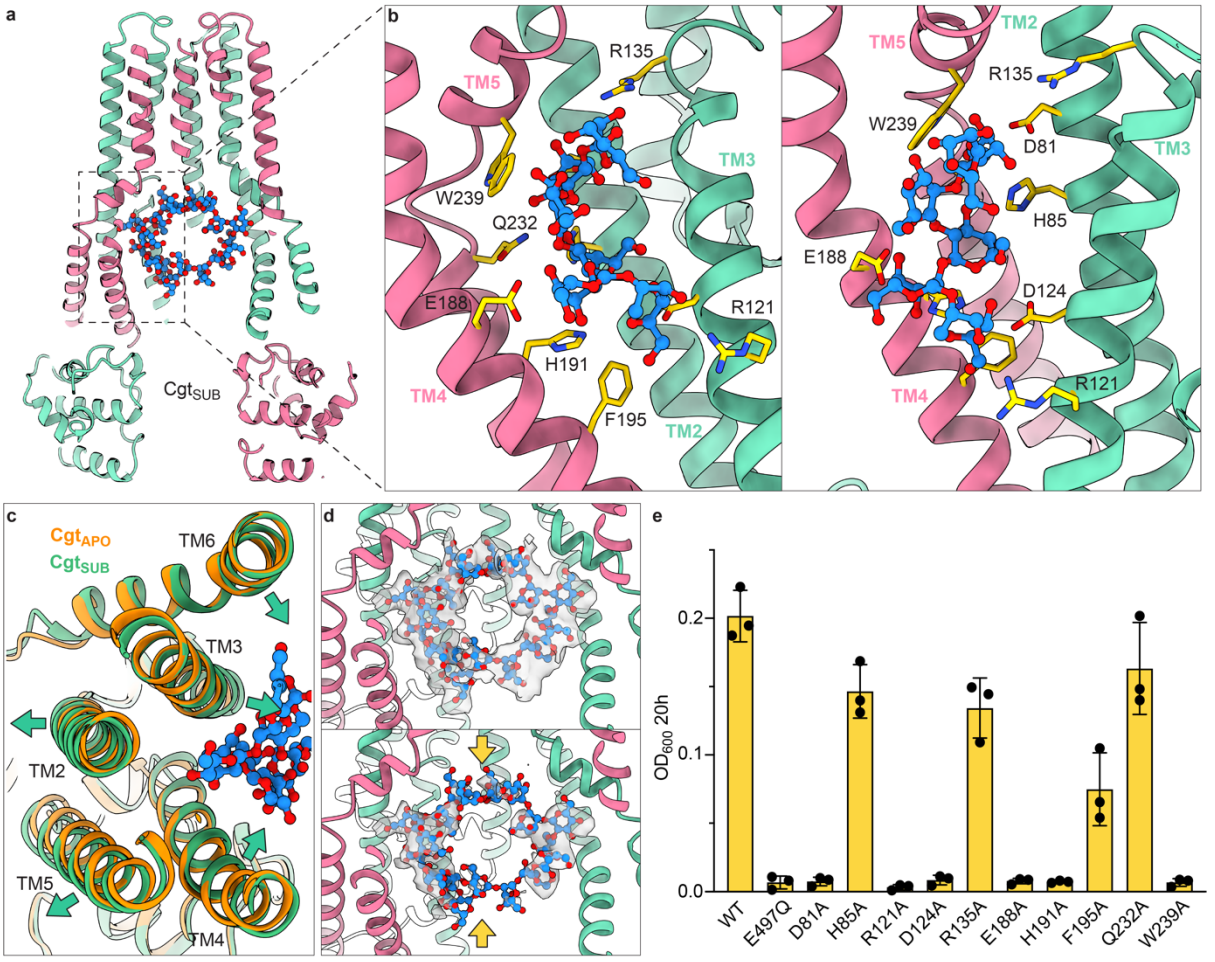

Fig. 3 | Substrate interaction of Cgt. a, Slice-through of the Cgt$_{SUB}$ model (pink, chain A; green, chain B), with an 18-mer CβG molecule (blue-red) bound in the central cavity. **b**, Side-view of a single CβG binding pocket at two angles. Residues forming the CβG binding interface are indicated with yellow sticks. The part of the CβG chain bound to the pocket is shown (blue-red). **c**, Top view of the CβG binding interface of superimposed Cgt$_{SUB}$ (green) and Cgt$_{APO}$ (orange) models. Substrate-induced movements of TM helices are indicated with arrows. **d**, Close up of the CβG molecule with the corresponding density map at two different contour level values (top: 0.15; bottom: 0.3). Arrows indicate flexible CβG fragments spanning the cavity. **e**, In-vivo Cgt activity assay. OD$_{600}$ values at 20 h time point. The ability of different point mutants of Cgt to restore growth of *Atu Δcgt* under osmotic stress indicates their importance in CβG binding. Dots represent mean values of independent experiments (n=3). Error bars represent standard deviation.

Despite lower overall quality resulting from strong preferred orientation, the Cgt$_{DET}$ map provides sufficient detail to reveal a distinct conformation of the TM helices, with a slight opening of the transporter towards the periplasmic side. This is achieved by the bending of TM1 and TM2 and the periplasmic loop connecting them, as well as lesser shifts of TM5 and TM6, leading to the opening of the isoleucine gate (Fig. 4b, Extended data Fig. 8c, d, Supp. Video 6). This partial opening differs from the outward-open structures previously reported for

type IV exporters, which are characterized by a strong rearrangement of TM1, TM2 and TM3[14-16], and could indicate an adaptation to glucan translocation. Both vanadate-bound conformations of Cgt are characterized by a large, flattened, highly polar central cavity, with the surface charge alternating several times along its length (Fig. 4c). Docking of the cyclic glucan substrate into the central cavity of the Cgt_{VAN} model indicates that it is sufficient to host a CβG molecule (Extended Data Fig. 8d). This volume partially overlaps with the unoccupied, inner part of the central cavity of the Cgt_{SUB} structure. This continuity could hint to a potential path for CβG translocation. We tested if a decrease in the size of the cavity in this path would affect Cgt function by introducing tryptophan substitutions of residues pointing inwards of the cavity in both conformations (Extended Data Fig. 9). Our results indicate that while single substitutions resulted in no to mild inhibition of Cgt activity, combinations of two substitutions mostly were detrimental.

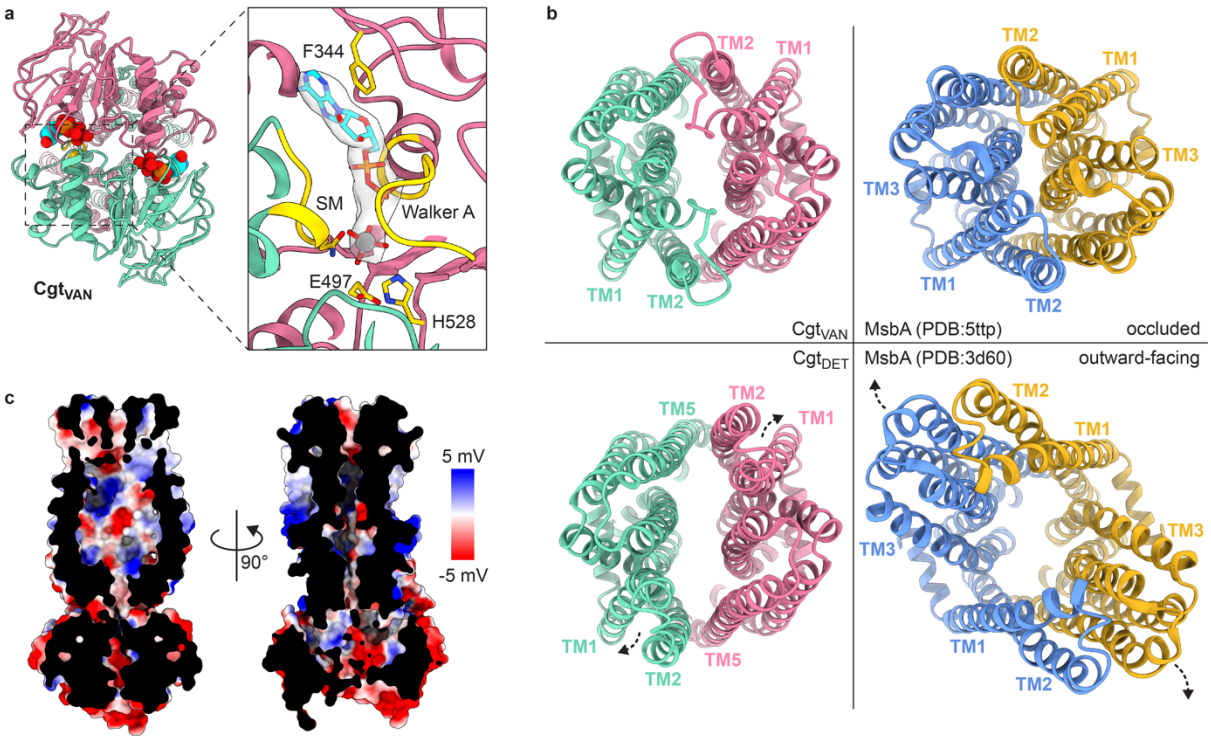

Fig. 4 | Nucleotide-bound Cgt. a, (left) bottom view of the NBDs dimer. ADP molecules and orthovanadate ions are shown as spheres. (right) Close-up of a single nucleotide binding pocket. The experimental densities corresponding to ADP and the vanadate ion are indicated (grey). Conserved motifs and residues responsible for the interaction are shown in yellow. Contour level is 1.2. **b**, top views of occluded (top) and outward-facing (bottom) models of Cgt (pink/green) and MsbA (blue/yellow). Arrows indicate the movements of TM helices leading to the opening of the central cavity to the periplasmic side. PDB IDs of MsbA models are indicated. **c**, Slice-through of the surface representation of Cgt_{VAN} at two different angles, colored according to electrostatic potential.

Discussion

In this study, we structurally characterized several conformations of Cgt and provided functional data in support of our structural analysis. The *in vitro* transport assay confirms Cgt as the exporter of CβGs and shows that it is sufficient for substrate recognition and translocation across lipid bilayers, while the *in vivo* activity assay clarifies the substrate interactions of the transporter.

Based on our data, we propose a model of substrate recognition and transport by Cgt (Fig. 5, Supp. Video 7). The reported structures account for steps 1 (Cgt_{APO}), 2 (Cgt_{SUB}), 4 (Cgt_{DET}) and 5 (Cgt_{VAN}), while step 3 corresponds to a short-lived, theoretical intermediate.

In the nucleotide-free state, the NBDs of Cgt are separated, and the large central cavity is facing the cytoplasm (step 1). CβG molecules are able to access the central cavity from the cytoplasm. Docking to Cgt requires a rearrangement of the glucan chain from a condensed solution state to an extended conformation that allows the interaction with the symmetric pockets (step 2).

Cgt lacks specialized carbohydrate-binding domains found in other transporters[17], which suggests that substrate recognition is mediated by this interface. This is supported by the observed sensitivity of the binding pockets to single amino acid substitutions. This combination of charged, polar and aromatic residues is similar to the pockets of known β-1,2-glucan-binding enzymes[18,19]. While parts of the CβG chain remain tightly associated with Cgt, the unbound parts of the sugar retain their flexibility. In vitro, Cgt displays a clear preference for 17- and 18-glucose chains, which represent a minor fraction at the lower end of the size distribution produced in vivo. However, as an accumulation of CβGs in the cytosol is likely detrimental for bacteria, all sizes produced must eventually be exported in vivo. We propose that upon binding to Cgt the larger polysaccharides adopt different conformations of their unbound parts, including potential supercoiling. This would facilitate their docking into the central cavity and

subsequent export. This mode of binding provides a balance between substrate specificity and size tolerance.

The dimerization of the NBDs induces the transition of Cgt into the outward-open state (steps 3, 4). Conformational changes in the TMs, including the straightening of TM5, disrupt the CβG binding interfaces, resulting in the movement of the glucan deeper into the central cavity. At this stage, the inner part of the cavity that remains unoccupied in the Cgt_{SUB} structure could provide additional space that allows the initial movement of the substrate towards the periplasmic space.

It has been suggested that highly polar surfaces facilitate polysaccharide translocation, since they provide extensive hydrogen bonding between protein side chains and hydroxyl groups of the sugar, which enables "sliding" of the polysaccharide without the need for desolvation of the sugar chain[20]. We propose that this mechanism drives CβG translocation along the polar central cavity of Cgt.

Our model indicates that the docking of the substrate in the central cavity as well as the subsequent dimerization of the NBDs require major conformational changes of the substrate (steps 2, 3). We suggest that the high activation energy associated with such rearrangements is a major bottleneck in the transporting cycle. This is likely the cause of lowered ATP turnover rates that we observed in the presence of CβG and bears resemblance to the kinetics of the transport of large peptides by TAPL[12]. The apparent *in vitro* preference of Cgt for smaller glucans might be yet another indication of an energy barrier related to substrate association.

Our outward-open conformation differs substantially from previous reports of type IV exporters[14-16]. It is characterized by more subtle shifts of TM helices and provides relatively less space constraints in the inner part of the cavity. This conformation could represent an alternative outward opening mechanism that allows accommodating large substrates. At this point, however, it is difficult to evaluate its biological relevance for the transporting cycle of

Cgt in particular or other type IV exporters. The release of the substrate leads to the outward occluded state (step 5), and the hydrolysis of ATP and nucleotide release reset the transporter to the initial conformation.

In summary, our report elucidates a number of specific adaptations of the entire transporting cycle of Cgt that allow accommodating a large polysaccharide cargo of varying size. These include a distinct glucan recognition and binding pocket located in a large, polar central cavity as well as a distinct outward-open conformation. Further insights into the specifics of Cgt transport process, its dynamics and substrate size preference, will improve the understanding of ABC transporter biology and, in more general terms, protein-polysaccharide interactions. In the context of microbiology research, the CβG synthesis pathway needs to be explored as a potential therapeutic target. While Cgm seems dispensable in the context of *Brucella* infection, both Cgt and Cgs were shown to play an important role[5], and might be better suited for drug development. The improved understanding of polysaccharide secretion mechanisms can equip us with tools to combat *Brucella*, as well as a variety of other pathogens that rely on glucan virulence factors.

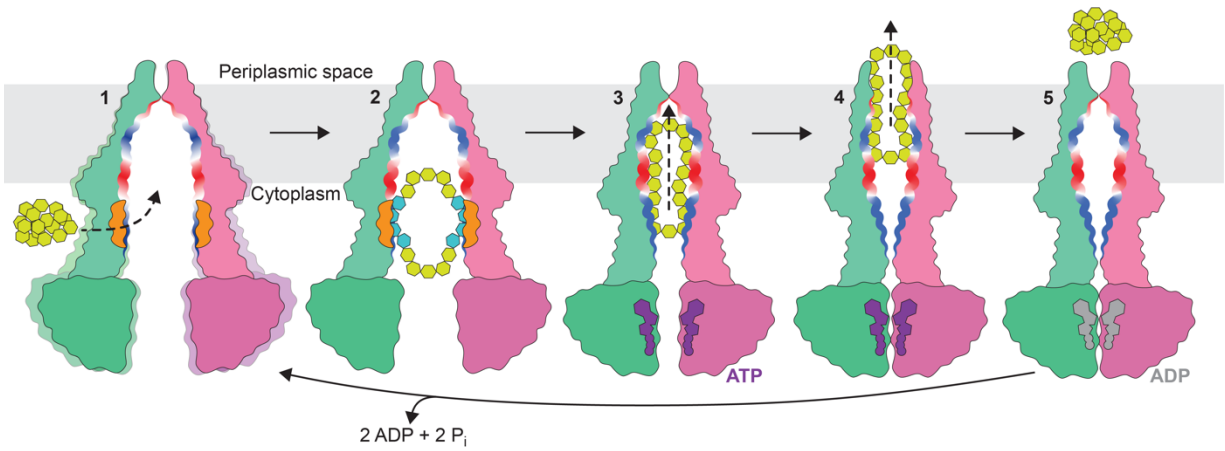

Fig. 5 | Model for CβG translocation by Cgt. Cgt monomers are indicated in pink and green. CβG is indicated in yellow, glucan chain parts interacting specifically with Cgt binding pockets are shown in cyan. CβG-binding pockets are colored in orange. Blue-red line indicates the alternating polarity of the central cavity. See text for a detailed description of the proposed transport cycle.

Acknowledgements

We thank M. Chami, K. N. Goldie, L. Kovacik and I. Mohammed from the BioEM Lab (University of Basel, Switzerland) for support during cryo-EM data collection. We thank C. Perez and G. Cebrero Acuña (University of Basel, Switzerland) for sharing their expertise in proteoliposome generation and handling. We thank L. Siewert for help during manuscript preparation. This work was supported by the Swiss National Science Foundation (SNSF, www.snf.ch) grant 310030B_201273 (to C.D.), SNSF NCCR AntiResist grant 180541 (to C.D.), SNSF NCCR TransCure grant 185544 (to H.S.) and the Chinese Scholarship Council (to N.W., Project 201709370040).

Author Contributions Statement

J.S., D.N and F.L. conceived the project and designed the experiments. J.S. and F.L. expressed and purified Cgt and MSP1D1 and reconstituted Cgt into lipidic nanodiscs and proteoliposomes. J.S. prepared cryo-EM grids. J.S. and D.N. performed cryo-EM data collection and processed electron microscopy data. D.N. built, refined and validated the structures. J.S. prepared DNA constructs, *A. tumefaciens* strains and carried out the functional assays. N.W. carried out the MAPDI-TOF experiments and data analysis. R.Z. provided resources and supervision to the MAPDI-TOF analysis. S.J. provided cyclic glucan samples. J.S and D.N. prepared the manuscript. C.D. and H.S. supervised the projects and participated in manuscript writing. All authors contributed to revision of the manuscript. Any correspondence should be to H.S. or C.D.

Competing Interests Statement

The authors declare no competing interests.

Tables

	Cgt_{VAN} (EMDB:14844) (PDB:7ZO9)	Cgt_{DET} (EMDB:14814) (PDB:7ZNU)	Cgt_{APO} (EMDB:14843) (PDB:7ZO8)	Cgt_{SUB} (EMDB:14845) (PDB:7ZOA)
Data collection and processing	60'975x (165kx)	60'975x (165kx)	60'975x (165kx)	60'975x (165kx)
Magnification	60'975x (165kx)	60'975x (165kx)	60'975x (165kx)	60'975x (165kx)
Voltage (kV)	300	300	300	300
Electron exposure (e–/Å^2)	70	70	70	70
Defocus range (μm)	0.8-2.8	0.8-2.8	0.8-2.8	0.8-2.8
Pixel size (Å)	0.82	0.82	0.82	0.82
Symmetry imposed	C2	C1	C1 / C2	C1 / C2
Initial particle images (no.)	1'729'641	575'806	1'680'729	2'772'136
Final particle images (no.)	75,311	196'351	383'591	379'991 / 185'149
Map resolution (Å)	3.5	4.0	3.6/3.4	4.0
FSC threshold	0.143	0.143	0.143	0.143
Map resolution range (Å)	30-3.50	30-4.10	30-3.50	30-3.50
Refinement				
Initial model used (PDB code)	n/a	n/a	n/a	n/a
Model resolution (Å) FSC threshold	0.143	0.143	0.143	0.143
Model resolution range (Å)	30-3.50	30-4.10	30-3.50	30-3.50
Map sharpening *B* factor (Å^2)	-162.9	-179.5	-156.1	-176.1
Model composition Non-hydrogen atoms Protein residues Ligands	 8886 1112 VO4: 2 BGC: 14 ADP: 2	 8730 1112 VO4: 2 ADP: 2	 8954 1140 LIG: 2	 9044 1140 BGC: 18
B factors (Å^2) Protein Ligand	 44.97/147.56/82.20 77.24/179.93/139.55	 57.80/219.76/114.28 99.40/102.35/99.63	 5.69/122.05/66.08 34.41/35.28/34.85	 89.89/318.16/167.09 157.48/195.84/170.27
R.m.s. deviations Bond lengths (Å) Bond angles (°)	 0.004 (0) 0.639 (10)	 0.003 (0) 0.635 (10)	 0.003 (0) 0.574 (10)	 0.003 (0) 0.679 (10)
Validation MolProbity score Clashscore Poor rotamers (%)	 2.01 10.77 0.00	 1.71 9.35 0.00	 1.81 8.35 0.42	 1.74 9.74 0.00
Ramachandran plot Favored (%) Allowed (%) Disallowed (%)	 92.69 7.13 0.18	 96.66 3.16 0.18	 94.89 4.75 0.35	 96.48 3.17 0.35

Table 1 | Cryo-EM data collection, refinement and validation statistics.

References

1. Ghanbari, M.K., et al., *One health approach to tackle brucellosis: a systematic review.* Trop Med Health, 2020. **48**: p. 86.
2. Pappas, G., et al., *The new global map of human brucellosis.* Lancet Infect Dis, 2006. **6**(2): p. 91-9.
3. Sedzicki, J., et al., *3D correlative electron microscopy reveals continuity of Brucella-containing vacuoles with the endoplasmic reticulum.* J Cell Sci, 2018. **131**(4).
4. Ben-Tekaya, H., J.P. Gorvel, and C. Dehio, *Bartonella and Brucella--weapons and strategies for stealth attack.* Cold Spring Harb Perspect Med, 2013. **3**(8).
5. Roset, M.S., et al., *Brucella cyclic beta-1,2-glucan plays a critical role in the induction of splenomegaly in mice.* PLoS One, 2014. **9**(7): p. e101279.
6. Breedveld, M.W. and K.J. Miller, *Cyclic beta-glucans of members of the family Rhizobiaceae.* Microbiol Rev, 1994. **58**(2): p. 145-61.
7. Mi, W., et al., *Structural basis of MsbA-mediated lipopolysaccharide transport.* Nature, 2017. **549**(7671): p. 233-237.
8. Bi, Y., et al., *Architecture of a channel-forming O-antigen polysaccharide ABC transporter.* Nature, 2018. **553**(7688): p. 361-365.
9. Cangelosi, G.A., G. Martinetti, and E.W. Nester, *Osmosensitivity phenotypes of Agrobacterium tumefaciens mutants that lack periplasmic beta-1,2-glucan.* J Bacteriol, 1990. **172**(4): p. 2172-4.
10. Ritchie, T.K., et al., *Chapter 11 - Reconstitution of membrane proteins in phospholipid bilayer nanodiscs.* Methods Enzymol, 2009. **464**: p. 211-31.
11. Ciocchini, A.E., et al., *A glycosyltransferase with a length-controlling activity as a mechanism to regulate the size of polysaccharides.* Proc Natl Acad Sci U S A, 2007. **104**(42): p. 16492-7.
12. Bock, C., et al., *Peptide translocation by the lysosomal ABC transporter TAPL is regulated by coupling efficiency and activation energy.* Sci Rep, 2019. **9**(1): p. 11884.
13. Kim, Y., et al., *Solubility Enhancement of Atrazine by Complexation with Cyclosophoraose Isolated from Rhizobium leguminosarum biovar trifolii TA-1.* Polymers (Basel), 2019. **11**(3).
14. Perez, C., et al., *Structure of Outward-Facing PglK and Molecular Dynamics of Lipid-Linked Oligosaccharide Recognition and Translocation.* Structure, 2019. **27**(4): p. 669-678 e5.
15. Ward, A., et al., *Flexibility in the ABC transporter MsbA: Alternating access with a twist.* Proc Natl Acad Sci U S A, 2007. **104**(48): p. 19005-10.
16. Dawson, R.J. and K.P. Locher, *Structure of the multidrug ABC transporter Sav1866 from Staphylococcus aureus in complex with AMP-PNP.* FEBS Lett, 2007. **581**(5): p. 935-8.
17. Mann, E., et al., *The Klebsiella pneumoniae O12 ATP-binding Cassette (ABC) Transporter Recognizes the Terminal Residue of Its O-antigen Polysaccharide Substrate.* J Biol Chem, 2016. **291**(18): p. 9748-61.
18. Tanaka, N., et al., *Identification, characterization, and structural analyses of a fungal endo-beta-1,2-glucanase reveal a new glycoside hydrolase family.* J Biol Chem, 2019. **294**(19): p. 7942-7965.
19. Abe, K., et al., *Structural and thermodynamic insights into beta-1,2-glucooligosaccharide capture by a solute-binding protein in Listeria innocua.* J Biol Chem, 2018. **293**(23): p. 8812-8828.
20. Dong, C., et al., *Wza the translocon for E. coli capsular polysaccharides defines a new class of membrane protein.* Nature, 2006. **444**(7116): p. 226-9.

Methods

Plasmids. All DNA ligations were performed using the In-Fusion HD Cloning Kit (Takara Bio). The identity of all constructs and mutant strains was confirmed by sequencing (Microsynth AG). Derivatives of pET22b were used for *E. coli* protein expression. pET22b backbone was PCR-amplified using primers prJS714 and prJS665 and the resulting product was digested using NdeI restriction enzyme (New England Biolabs). *Brucella abortus* 2308 *cgt* gene (*ndvA*) was PCR-amplified from heat-killed colonies using primers prJS205 and prJS1074. Both fragments were ligated resulting in plasmid pJS177. Plasmid pJS197 was generated by PCR-amplifying pJS177 with primers prJS868 and prJS869 and re-ligating the PCR product. To generate plasmid pJS290, DNA fragments upstream and downstream of the *chvA* gene were amplified from heat-killed *A. tumefaciens* colonies using primer pairs prJS769/prJS770 and prJS936/prJS937. The fragments were then ligated into the pnPTS138 backbone digested with SalI and HindIII. To generate pBBR1-MCS2 derivatives used for *A. tumefaciens* gene expression, the main pBBR1-MCS2 plasmid backbone was amplified using primers prJS893 and prJS1007. Region upstream containing the putative promoter region of *Atu cgt* (*chvA*) was amplified with primers prJS769 and prJS1013. *Bab cgt* gene was amplified from pJS177 using primers prJS1014 and prJS1075. All three fragments were ligated to generate pJS461. To mimic the original genomic sequence of *B. abortus*, GTG was used as the start codon. To generate the pJS420 empty vector, the same promoter region was amplified using primers prJS769 and prJS1016 and ligated with the pBBR1 vector. To generate pJS461 derivatives with mutated variants of *Bab cgs* gene, the entire plasmid pJS461 was amplified using mutagenesis primer pairs, followed by re-ligation. The full list of primers used in the study is specified in Supplementary Table 1. The generated plasmids are specified in Supplementary Table 2.

Bacteria strains. Stellar competent cells (Takara Bio) provided with the In-Fusion Cloning Kit were used in all cloning procedures. All strains were maintained in lysogeny broth (LB, 10 g l^{-1} tryptone, 5 g l^{-1} yeast extract, 10 g l^{-1} NaCl). When required, ampicillin (200 μg ml^{-1}), kanamycin (50 μg ml^{-1}) and 5-aminolevulinic acid (50 μg ml^{-1}) were added to growth media. C43(DE3) *E. coli* strain (Lucigen) was used for large scale protein expression. All *E. coli* strains were grown at 37°C unless stated otherwise. *A. tumefaciens* C58 strains were cultivated at 28°C. All plasmids were introduced into *Atu* strains by conjugation using the ST18 donor strain[21]. To generate *A. tumefaciens cgt* deletion strain (*Atu Δcgt*), pJS290 was conjugated into *Atu* C58 parental strain. Clones that have undergone two successful recombination events were

selected in a two-step process. The deletion of the *chvA* locus encoding the *cgt* gene was confirmed by sequencing. Strains used in growth assays were generated by conjugating the empty plasmid pJS420 or pJS461 and its derivatives carrying point mutations into *Atu Δcgt* (see Table 3 for the full list of plasmids used). The expression of the *cgt-3xFlag* constructs in the resulting *Atu* strains was confirmed by Western blot using an anti-Flag antibody (Sigma).

***Atu* growth assay.** *Atu* strains were precultured overnight at 28°C in 14 ml PP tubes (Sarstedt) in a rotary shaker. The OD_{600} of the cultures was measured in a BioPhotometer #6131 (Eppendorf). The cultures were then used to inoculate YPL medium (0.1% peptone, 0.1% yeast extract, 0.09% glucose) at a final OD_{600} of 0.01. The cultures were then dispensed into 96-well flat bottom plate (160 µl per well) and placed Synergy H4 Hybrid Microplate Reader (BioTec) and incubated with fast shaking at 28°C for indicated periods of time. OD600 was measured every 60 min. If needed, 5 M NaCl was added to the YPL medium to a final concentration of 15 or 100 mM. Technical well duplicates were used for each strain. Each reported result represents at least 3 (n=3) biological replicates.

Cgt expression and purification. Chemocompetent *E. coli* C43 cells were transformed with plasmids pJS177 or pJS197 and grown overnight on LA plates supplemented with 10 mg ml^{-1} glucose. The following day, colonies were used to inoculate pre-cultures in TB medium supplemented with 10 g l^{-1} glucose. The following morning, large scale TB medium cultures were inoculated in baffled flasks and grown until OD600 of 1.5-1.7 and induced with 1 mM IPTG. After overnight culture at 20°C, the cells were collected by centrifugation and frozen at -80°C until further processing. All purification steps were performed at 4°C. Bacteria pellets were resuspended in lysis buffer (50 mM HEPES pH 7.5, 500 mM NaCl) supplemented with cOmplete protease inhibitor tablets (Roche) and lysed by 3 passes at 20'000 psi through a microfluidizer (Microfluidics). Large debris was removed by centrifugation (30 min, 10,000g) and cell membranes were pelleted by ultracentrifugation (45 min, 200,000g). Membrane pellets were solubilized with 1% n-dodecyl-β-d-maltopyranoside (DDM, Anatrace), loaded onto Flag affinity agarose beads (Sigma) and washed extensively with buffer containing 0.05% DDM. For LMNG samples, DDM was replaced with 0.001% LMNG (Anatrace) for the final washes and elution. Following elution with 0.4mg/mL 3xFlag peptide (Sigma), the samples were purified by size-exclusion chromatography on a Superose 6 Increase 10/300 column (GE Healthcare).

Reconstitution of Cgt into nanodiscs. *E. coli* polar lipid extract (Avanti Polar Lipids) was solubilized in chloroform, dried under nitrogen gas to form a lipid film, and stored under

vacuum overnight. The lipid film was resuspended at a concentration of 25 mM in buffer containing 20 mM HEPES, pH 7.5, 150 mM NaCl and 300 mM sodium cholate. Purified Cgt, the MSP1D1 membrane scaffold protein[10] and lipids were mixed at a molar ratio of 1:4:100 in buffer containing 25 mM HEPES, pH 7.5, 150 mM NaCl and incubated for 30 min. at 4°C. Detergents were removed by incubation with 100 mg Bio-Beads SM2 (Bio-Rad) overnight at 4°C. The Cgt-nanodisc complexes were purified using a Superose 6 Increase 10/300 column (GE Healthcare) in a buffer containing 25 mM HEPES, pH 7.5, and 150 mM NaCl.

Reconstitution of Cgt into proteoliposomes. *E. coli* polar lipids at a concentration of 10 mg ml^{-1} in 25 mM HEPES pH 7.5, 100mM NaCl were extruded through a 400 nm filter to generate liposomes. Purified Cgt_{WT} at a concentration of 2 mg ml^{-1} was added to liposomes destabilized by 0.3% DDM at a 50:1 lipid:protein ration (w:w). Detergent was then removed by four rounds of fresh Bio-Beads. Resulting proteoliposomes were washed by centrifugation (110'000 g, 4°C, 30 min.). The incorporation of Cgt into proteoliposomes was confirmed by SDS-PAGE. Empty control liposomes were generated following the same protocol without the addition of protein.

Purification of cyclic β-1,2-glucans. Cyclic β-1,2-glucans were isolated from *R. leguminosarum* supernatant and purified to homogeneity following the procedure described previously[13].

ATPase assay. ATP turnover rate was measured for both WT and E497Q nanodisc-reconstituted Cgt using the malachite green-based ATPase Activity Assay Kit (Sigma). The measurements were performed in technical triplicates in flat-bottom 96-well plates in 40 µl reactions. The final concentrations were 8 µg ml^{-1} Cgt-nanodisc, 0.2 mM ATP, 0.25 mM $MgCl_2$, 50 mM HEPES, pH 7.5, 150 mM NaCl. After pipetting on ice, reactions were incubated for 20 min. at 22°C and stopped by adding 200 µl malachite green solution to each well. Following 45 min. of incubation at 22°C, absorbance at 520 nm was measured using the Spark Microplate Reader (Tecan). The final phosphate concentrations were calculated based on a standard curve generated with the phosphate solution provided with the kit. The results represent an average of 4 experiments (n=4).

Binding of CβG by Cgt-nanodiscs. 50 µl of purified, nanodisc-reconstituted Cgt_{E497Q} was incubated with 1.5 mM CβG or no additives for 20 min. at 22°C. The samples were then diluted with buffer to 500 µl and concentrated to 50 µl in a 50 kDa cutoff Amicon centrifugal filters (Merck). The dilution and concentration procedure was repeated 10 times. The samples were then concentrated to a final volume of 20 µl and subjected to mass analysis.

CβG uptake assay. Cgt proteoliposomes at a final lipid concentration of 5 mg ml^{-1} were used for the uptake assay. Proteoliposomes and control liposomes were incubated with 1mM CβG on ice for 5 min. The inhibited sample was additionally pre-incubated with 2 mM ATP and 2mM sodium orthovanadate for 10 min. at 22°C before adding the CβG. Following the addition of 5 mM ATP and 5 mM $MgCl_2$, the samples were incubated at 37°C for 45 min. with mild shaking. Afterwards, the buffer was exchanged four times by centrifugation (110'000 g, 4°C, 30 min.). The liposomes were then lysed by the addition of 0.2% DDM and multiple freeze-thaw cycles. The samples were run through Amicon 30 kDa cutoff Amicon centrifugal filters (Merck) to clear the remaining protein material, lipids and detergent micelles. Finally, the sample buffer was exchanged to water in 3 kDa cutoff Amicon centrifugal filters (Merck). The samples were then concentrated to a final volume of 30 µl and subjected to mass analysis.

MALDI-TOF mass spectroscopy analysis. All mass spectrometric data were obtained in linear positive ion mode on a MALDI-TOF/TOF mass spectrometer (model 4800 plus, AB Sciex, Darmatadt, Germany) equipped with a high-mass detector (HM2, CovalX AG, Zurich, Switzerland). MALDI was initiated by a Nd:YAG laser pulse (355 nm), and 500 shots per spectrum were accumulated. The samples were measured using sample preparation conditions optimized for low mass (for the detection of the glycans) or high mass (for the detection of the proteins). In low-mass mode, 50 mg/mL 2,5-dihydroxybenzoic acid (DHB, purchased from Sigma-Aldrich) were dissolved in a 1:500:500 v/v/v TFA/water/acetonitrile solution, and then mixed with the sample in a 1:1 volume ratio. 0.7 µL of each sample were then spotter onto the stainless steel MALDI plate and dried in air. In high-mass mode, 10 mg/mL sinapinic acid (Tokyo Chemical Industry, Eschborn) were dissolved in a 1:500:500 v/v/v TFA/water/acetonitrile solution, and then mixed with the samples in a 1:1 volume ratio. The high voltages HV1 and HV2 of the HM2 detector were set to −3.5 kV and −20.0 kV, respectively. Data was processed using Origin.

Electron microscopy sample preparation. Purified protein samples were concentrated to 0.8-1.0 mg ml^{-1} (LMNG sample) or 2.0-2.5 mg ml^{-1} (nanodisc-reconstituted samples). To generate the Cgt_{SUB} sample, purified CβG was added to the protein sample at a final concentration of 1 mM and incubated at 22°C for 15 min. directly before freezing. The Cgt_{VAN} and Cgt_{DET} samples were generated by incubating the protein sample with 1.5 mM ATP, 1.5 mM $MgCl_2$ and 1.5 mM sodium orthovanadate at 22°C for 15 min. directly before freezing. 4 µl of protein solution was applied to a glow-discharged Quantifoil holey carbon grid (2/2, 300 mesh). Grids were blotted for 3 s at 100% humidity and 4°C, using a Vitrobot Mark IV (ThermoFischer).

Electron microscopy data collection. Cryo-EM data were collected on a Titan Krios (ThermoFischer) operated at 300 kV and equipped with a Gatan Quantum-LS energy filter (20 eV zero loss energy filtration), and recorded with a K2 Summit direct electron detector (Gatan Inc., CA, USA). All movies were recorded using automated data collection software SerialEM[22]. Dose-fractionated (40 frames) images were acquired in super-resolution counting mode at nominal magnification of 160,000x, corresponding to a physical pixel size of 0.82 Å. The total dose was 70.0 electrons per $Å^2$, the total recording time per image was 4 seconds. Images were recorded with an underfocus ranging from -1.0 to -2.2 μm.

EM image processing. Dose-fractionated movies were subjected to motion corrected with MotionCor2[23] integrated into the Focus package[24]. All subsequent processing steps were performed using cryoSparc software[25]. Defocus values were estimated in the aligned-average images using CTFFIND4[26]. For details regarding the processing workflow, see Table 1 and Extended Data Fig. 3-6.

Tilting cryo-EM. For the sample of Cgt_{DET}, a strong preferred orientation was present. The grid tilting approach was applied to the data collection with rotation angles of 0^o, 30^o and 60^o. The data processing strategy was largely identical to that of the remaining datasets apart from the method of CTF correction. The defocus and CTF values were measured by the patch-based CTF estimation tool in cryoSparc[25].

Model building and refinement. The resulting cryo-EM maps allowed mostly de novo modeling of the atomic structures. Firstly, the Cgt_{VAN} structure was built as the densities were excellent in both TM domains and NBD regions. An initial pdb file was generated by SWISS-MODEL[27], for which the second half of the ABCB1 (PDB: 6C0V) pseudo-dimer structure was used as a template[28]. The initial model was rigid-body docked into the 3D map obtained from the Cgt_{VAN} sample as two halves using UCSF Chimera[29]. Model rebuilding was performed in Coot 0.9.4[30]. Backbone (C-alpha) of TM domains and NBDs were manually adjusted and the protein sequence was re-registered against densities. Two copies of ADP molecules and orthovanadate ions were auto-weighting docked into the ATP binding sites and no Mg2+ ion was found around the vanadate binding positions. Additional densities were found in the middle of TM4 and TM1a, which we built as the partial β-1,2-glucan chain. For the Cgt_{DET} structure, the newly rebuilt Cgt_{VAN} model was initially rigid-body docked as a dimer. Subsequently, the TM1/TM2, L1/2, L5/6 regions from each monomer were refitted using Coot and the remaining parts were adjusted. For Cgt_{APO} structure, the model adapted from the Cgt_{VAN} model was pre-docked into the 3D map and rebuilt specifically for regions such as the

TM4 and TM5. In addition to transmembrane domains, the NBD regions were rigid-body refitted with a resolution limit of 5~ Å. For Cgt_{SUB} structure, the starting model adapted from the Cgt_{APO} structure was docked into the density using the trimmings>fitting plugin in Coot[30]. The closed cyclic β-1,2-glucan 18-mer was manually built into the additional density that was present in the central cavity. All the newly built atomic models were refined in Phenix using the program real_space_refine[31] with general parameters to order to optimize the structural geometry. The model quality assessment was estimated with Phenix, Comprehensive validation[32] and Molprobity[33] (web server). Structure refinement statistics are listed in Table 1.

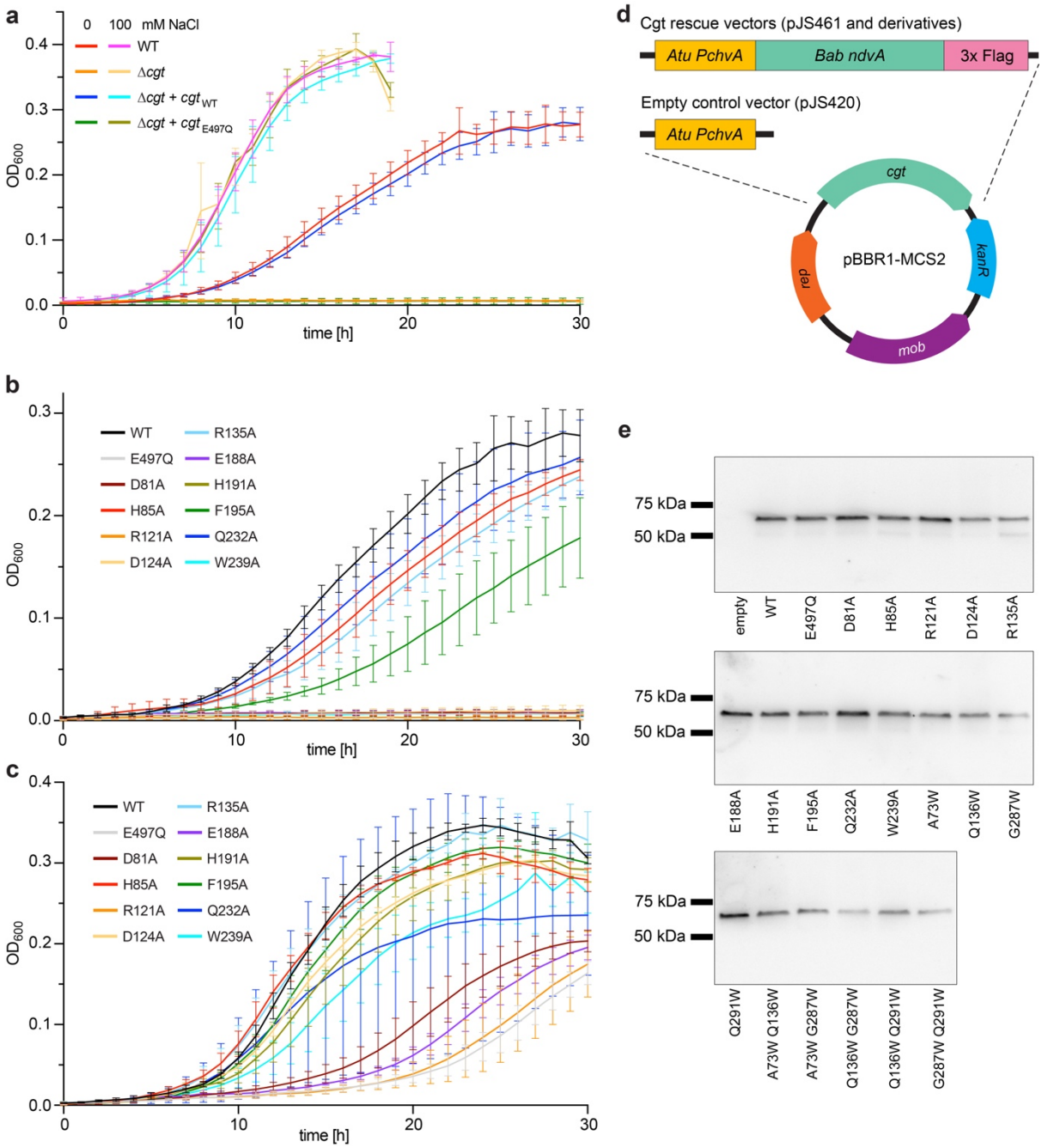

Extended Data Fig. 1 | In vivo Cgt activity assay. a, Growth dynamic of *Atu* under osmotic stress. The *Δcgt* mutant can be rescued with WT *B. abortus cgt* gene, but not with cgt_{E497Q}. Addition of 100 mM NaCl restores growth of all strains. **b,** *Atu Δcgt* was rescued with different point mutants of *Bab cgt* under low osmotic stress conditions (YPL). **c**, Same as b, with low osmotic stress partially alleviated by the addition of 15 mM NaCl to the medium. **d**, Cartoon representation of the constructs used in the assay. **e**, Western blot analysis of *cgt-3xFlag* gene expression in *Atu* strains used in the assay. All growth curves represent mean values of 3 independent experiments (n=3). Error bars represent standard deviation. Data for graphs a-c and uncropped images for e are available as source data. Western blot analysis was performed once (n=1).

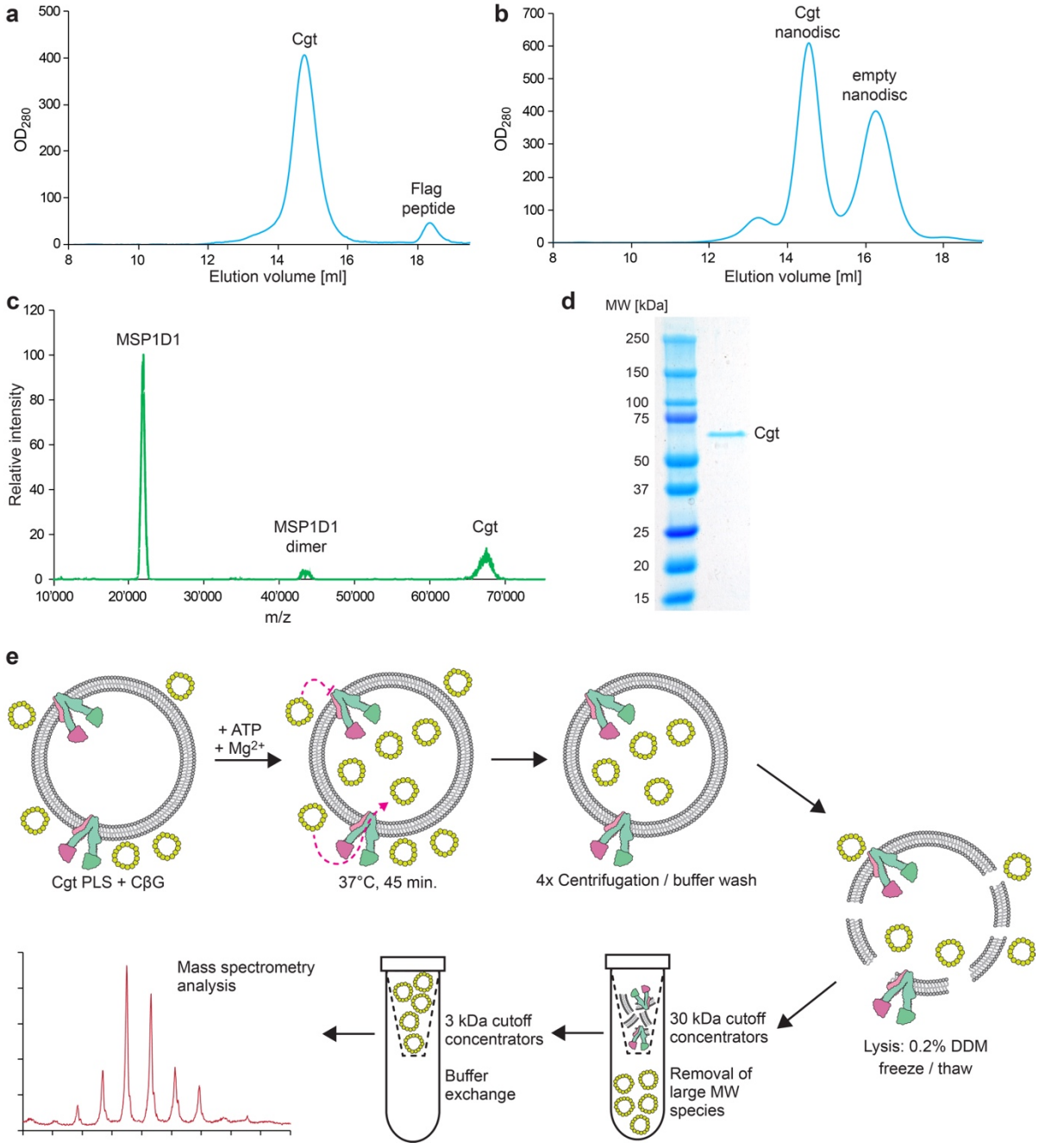

Extended Data Fig. 2 | Purification of Cgt in LMNG and nanodiscs. a, Gel-filtration profile (Superose 6 Increase 10/300) of Cgt in LMNG. **b,** Gel-filtration profile (Superose 6 Increase 10/300) of Cgt in nanodiscs formed by MSP1D1 and *E. coli* polar lipids. **c,** MALDI-TOF analysis of Cgt in nanodiscs, indicating the presence of Flag-tagged Cgt (68.7 kDa) and MSP1D1 (22 kDa) in the sample. **d**, SDS-PAGE of Cgt proteoliposome sample indicating the incorporation of Flag-tagged Cgt (68.7 kDa). **e**, Diagram describing the CβG proteoliposome uptake assay. See the Methods section for the description. Mass spectroscopy data for c and uncropped gel image for d are available as source data. SDS-PAGE analysis was performed once (n=1)

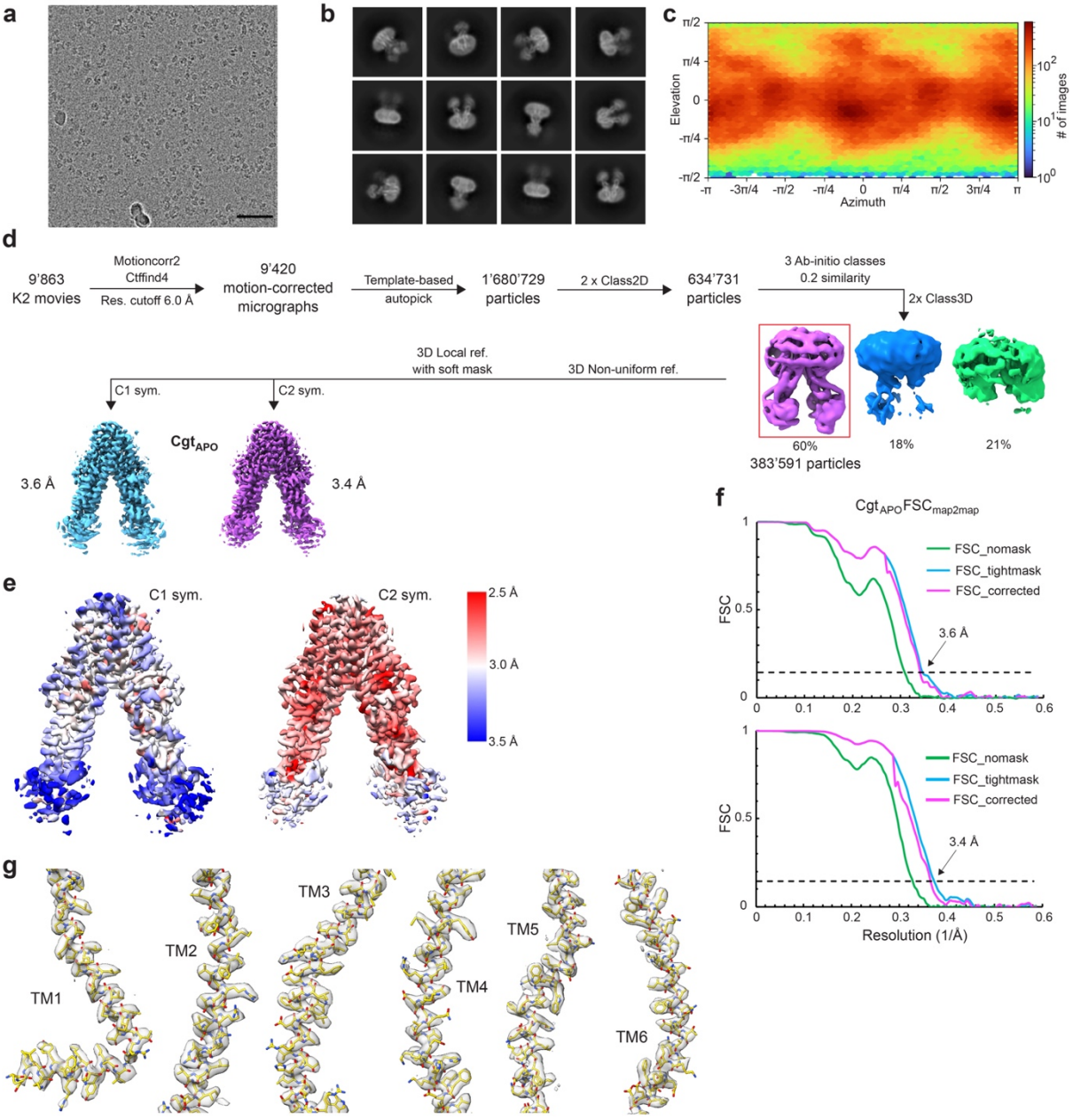

Extended Data Fig. 3 | Cryo-EM data processing workflow for nanodisc-stabilized Cgt$_{E497Q}$ substrate-free structure (Cgt$_{APO}$). a, Representative motion-corrected cryo-EM micrograph (scale bar is 50 nm). **b**, representative 2D class averages. **c**, Angular distribution of the cryo-EM particles included in the final reconstruction. **d**, Single-particle cryo-EM data processing scheme using cryoSparc 3.1. **e**, Final 3D reconstruction colored according to local resolution. **f**, Fourier shell correlation curves for the final 3D reconstruction. **g**, TM helices of the Cgt$_{APO}$ model overlapping with the corresponding experimental density. Contour levels are 1.0. Cryo-EM data was obtained in a single data collection session (n=1).

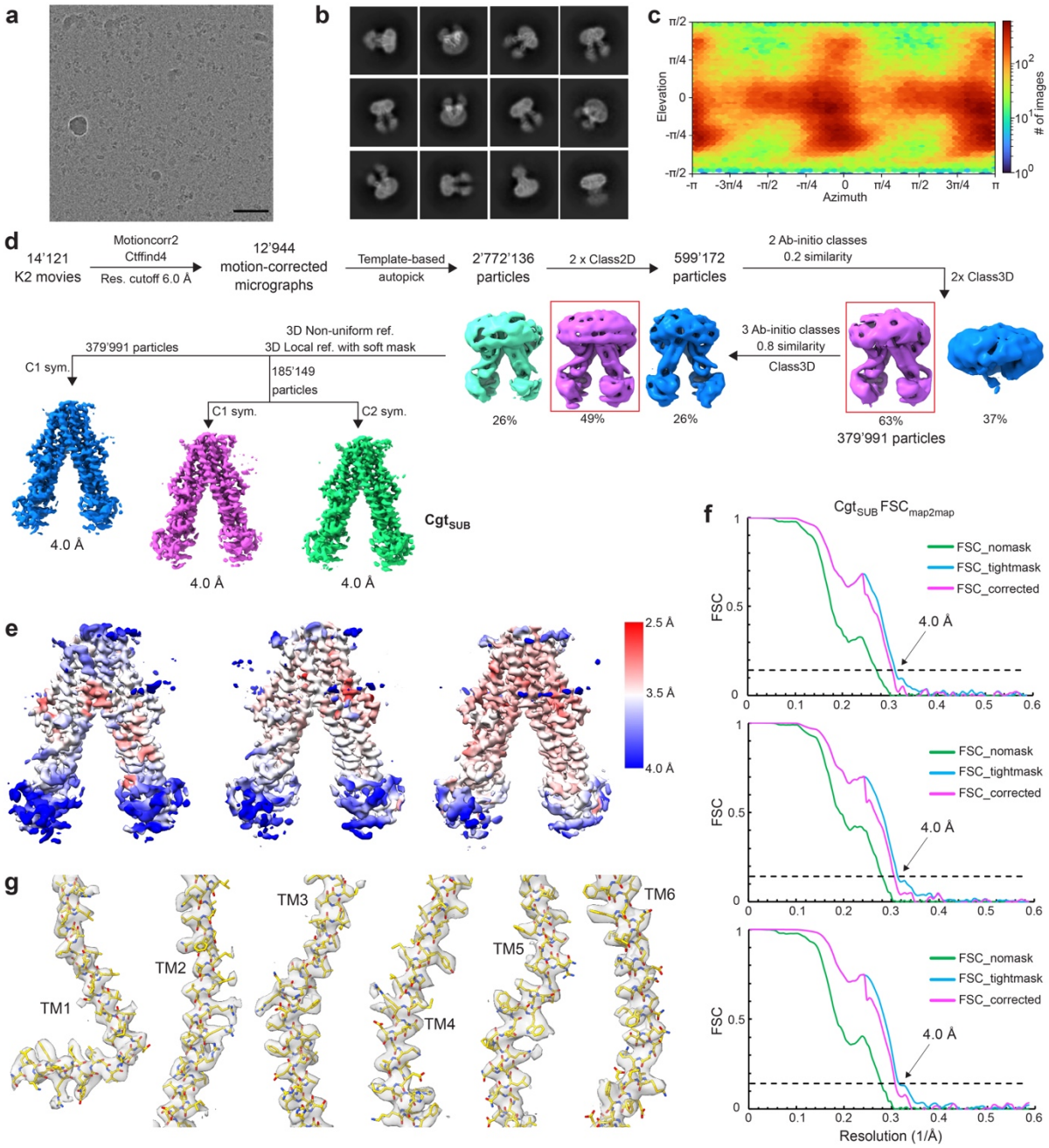

Extended Data Fig. 4 | Cryo-EM data processing workflow for nanodisc-stabilized Cgt$_{E497Q}$ with CβG substrate (Cgt$_{SUB}$). a, Representative motion-corrected cryo-EM micrograph (scale bar is 50 nm). **b**, representative 2D class averages. **c**, Angular distribution of the cryo-EM particles included in the final reconstruction. **d**, Single-particle cryo-EM data processing scheme using cryoSparc 3.1. **e**, Final 3D reconstruction colored according to local resolution. **f**, Fourier shell correlation curves for the final 3D reconstruction. **g**, TM helices of the Cgt$_{SUB}$ model overlapping with the corresponding experimental density. Contour levels are 0.5. Cryo-EM data was obtained in two data collection sessions (n=2).

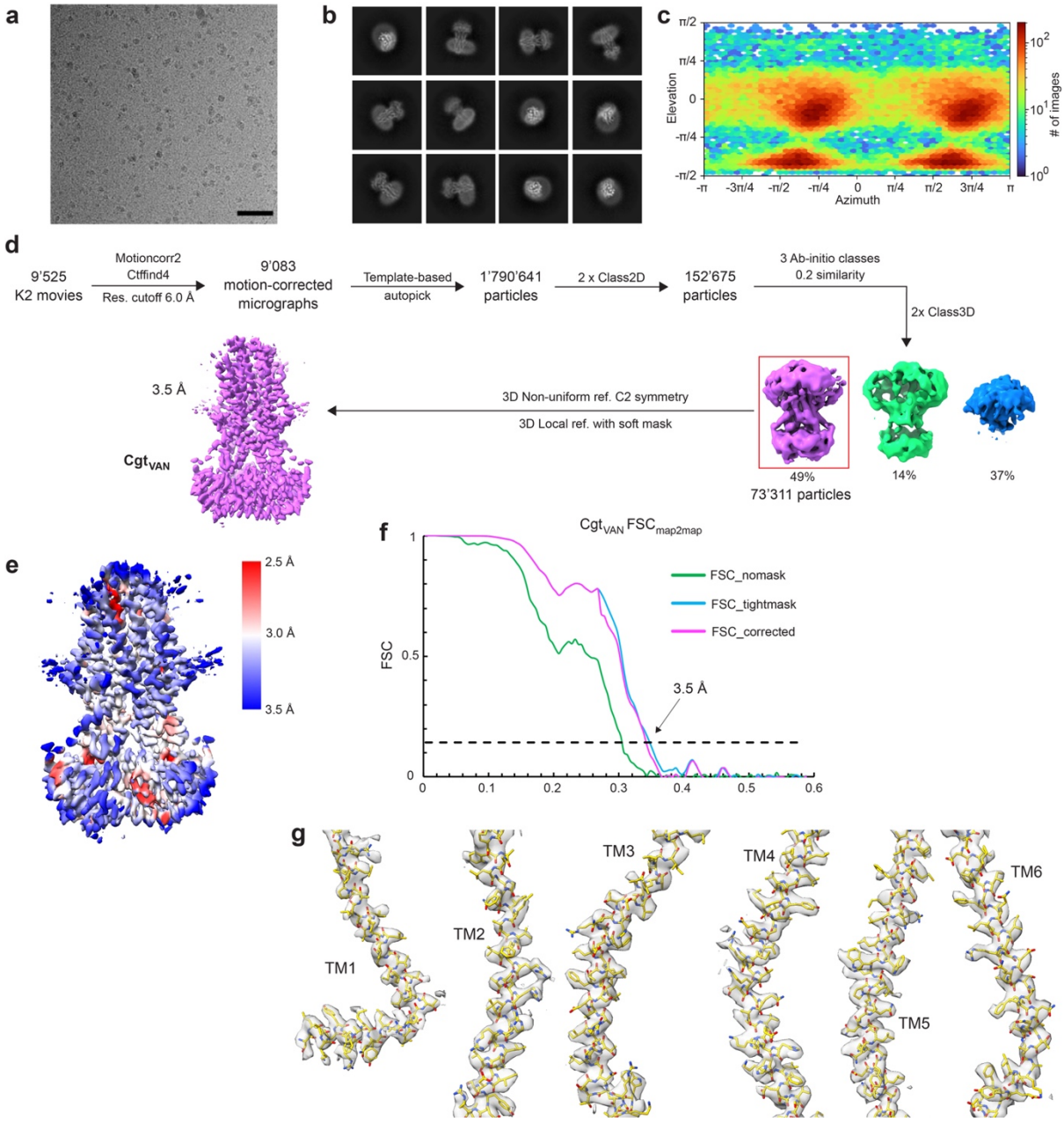

Extended Data Fig. 5 | Cryo-EM data processing workflow for nanodisc-stabilized Cgt_{WT} with Mg^{2+}, ADP, sodium orthovanadate and CβG (Cgt_{VAN}). a, Representative motion-corrected cryo-EM micrograph (scale bar is 50 nm). **b**, representative 2D class averages. **c**, Angular distribution of the cryo-EM particles included in the final reconstruction. **d**, Single-particle cryo-EM data processing scheme using cryoSparc 3.1. **e**, Final 3D reconstruction colored according to local resolution. **f**, Fourier shell correlation curves for the final 3D reconstruction. **g**, TM helices of the Cgt_{VAN} model overlapping with the corresponding experimental density. Contour levels are 0.5. Cryo-EM data was obtained in a single data collection session (n=1).

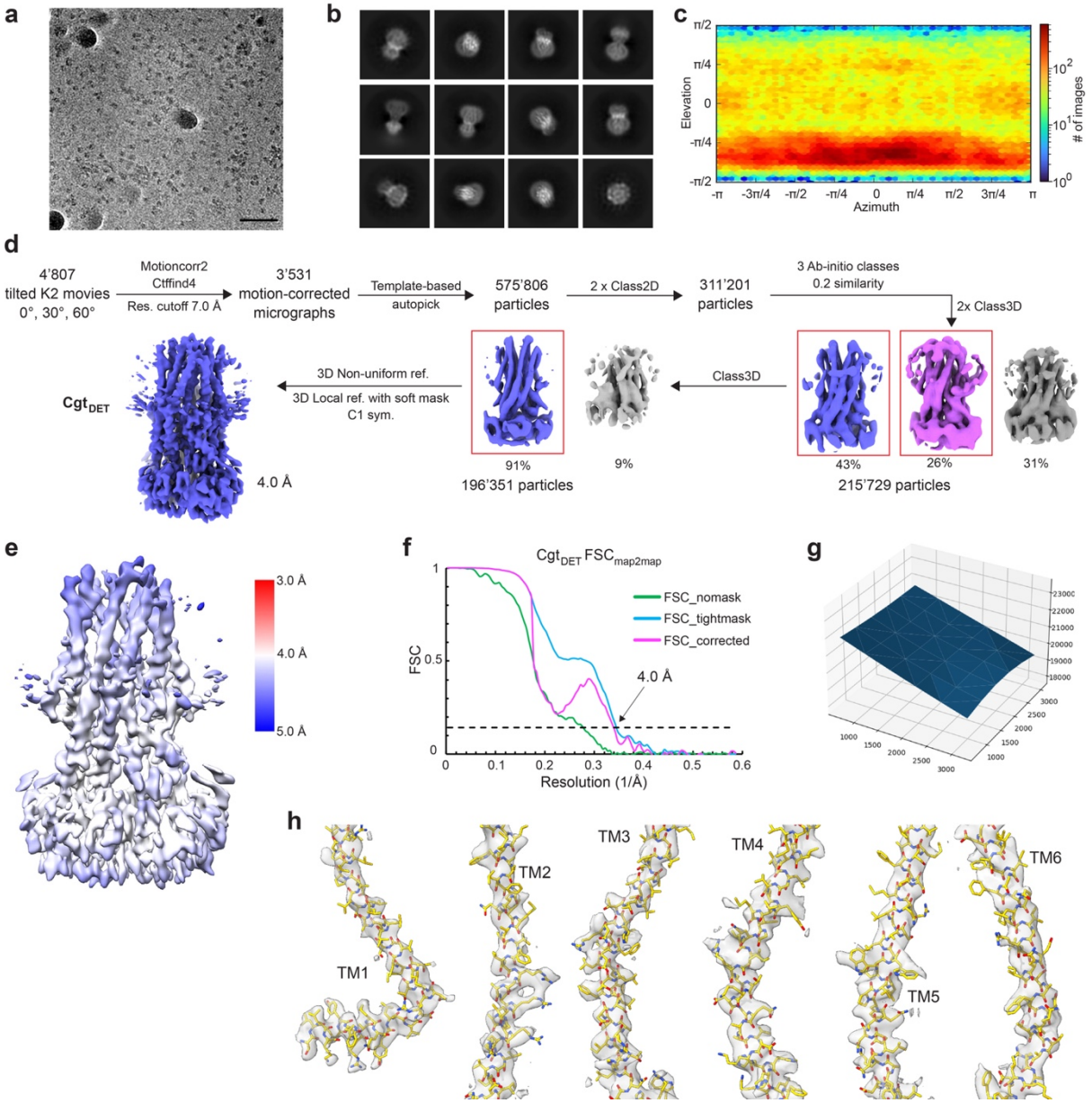

Extended Data Fig. 6 | Cryo-EM data processing workflow for LMNG-solubilized Cgt$_{WT}$ with Mg^{2+}, ADP, sodium orthovanadate and CβG (Cgt$_{DET}$). a, Representative motion-corrected cryo-EM micrograph (scale bar is 50 nm). **b**, representative 2D class averages. **c**, Angular distribution of the cryo-EM particles included in the final reconstruction. **d**, Single-particle cryo-EM data processing scheme using cryoSparc 3.1. **e**, Final 3D reconstruction colored according to local resolution. **F**, Fourier shell correlation curves for the final 3D reconstruction. **g**, Local defocus values (Å) for an example micrograph indicating the sample tilt. **h,** TM helices of the Cgt$_{VAN}$ model overlapping with the corresponding experimental density. Contour levels are 0.4. Cryo-EM data was obtained in a single data collection session (n=1).

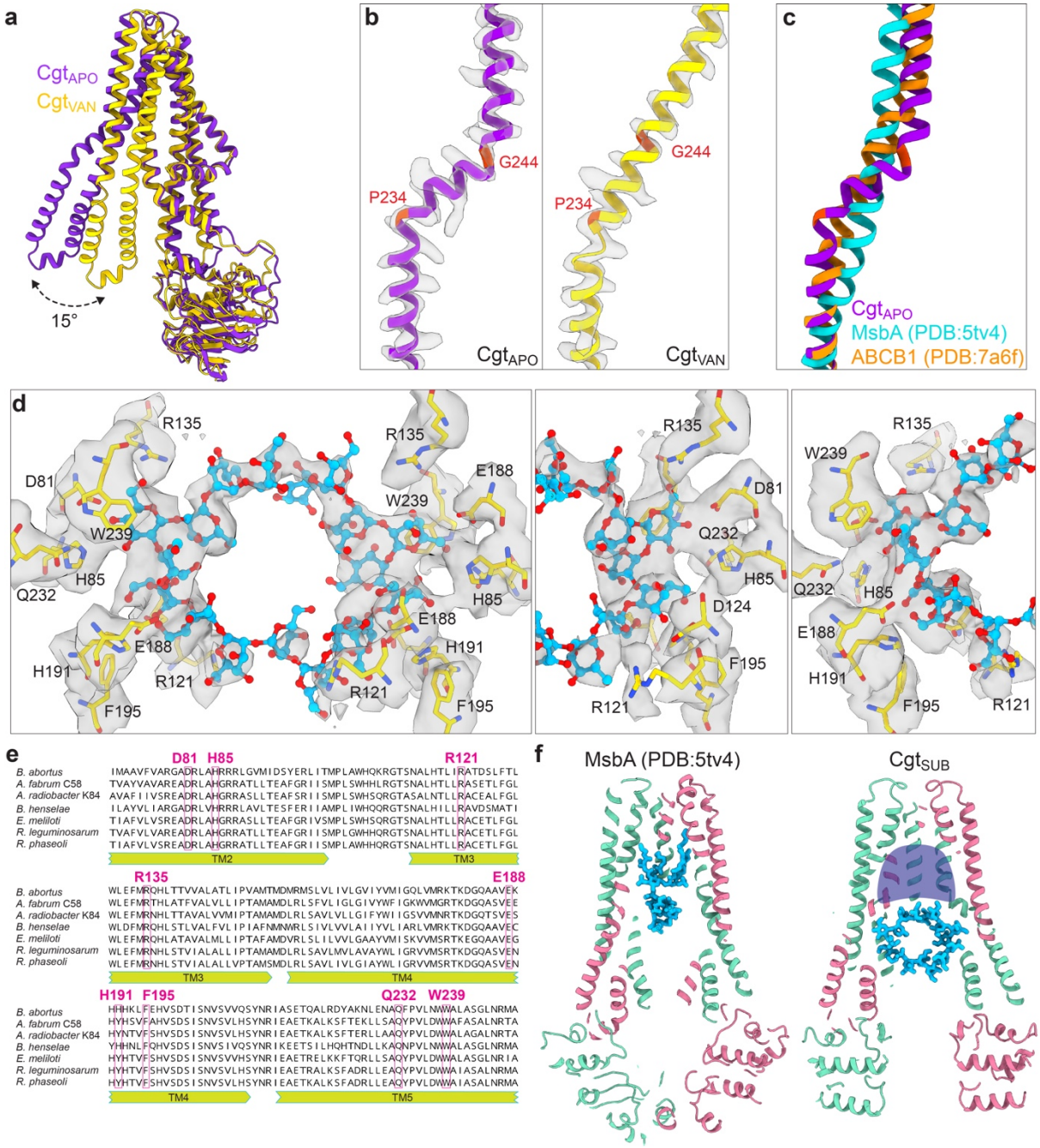

Extended Data Fig. 7 | Inward-facing conformations of Cgt. a, Alignment of single monomers of Cgt_{APO} (purple) and Cgt_{VAN} (yellow), indicating the hinging movement of TM helices 4 and 5 that allows the transition between conformational states. **b**, Comparison of TM5 of Cgt_{APO} (left) and Cgt_{VAN} (right) models. Corresponding density maps are shown. Residues P234 and G244 facilitating the bending of the helix are shown in red. Contour levels are 1.9 and 1.0. **c**, Alignment of TM5 of Cgt with its structural homologues. Purple, Cgt TM5; blue, TM5 of MsbA (PDB:5tv4); orange, TM11 of ABCB1 (PDB:7a6f). **d,** Overlay of the Cgt_{SUB} cryo-EM density map with the corresponding model at three different angles. An 18-glucose CβG molecule is shown in blue/red. Residues forming the substrate-binding pocket are shown in yellow. Contour levels are 0.25. **e**, Alignment of Cgt sequences from different species of Rhizobiales focusing on the substrate-binding pocket area. *B. abortus* residues described in this study are marked with magenta. Sequences corresponding to transmembrane helices are marked in green. Alignment was generated using Geneious. **f**, Slice-through views of the substrate-bound models of MsbA (PDB:5tv4, left) and Cgt_{SUB} (right), indicating distinct substrate-binding mechanisms. Respective substrates are indicated in blue. Unoccupied, inner part of the Cgt central cavity is indicated with blue shading.

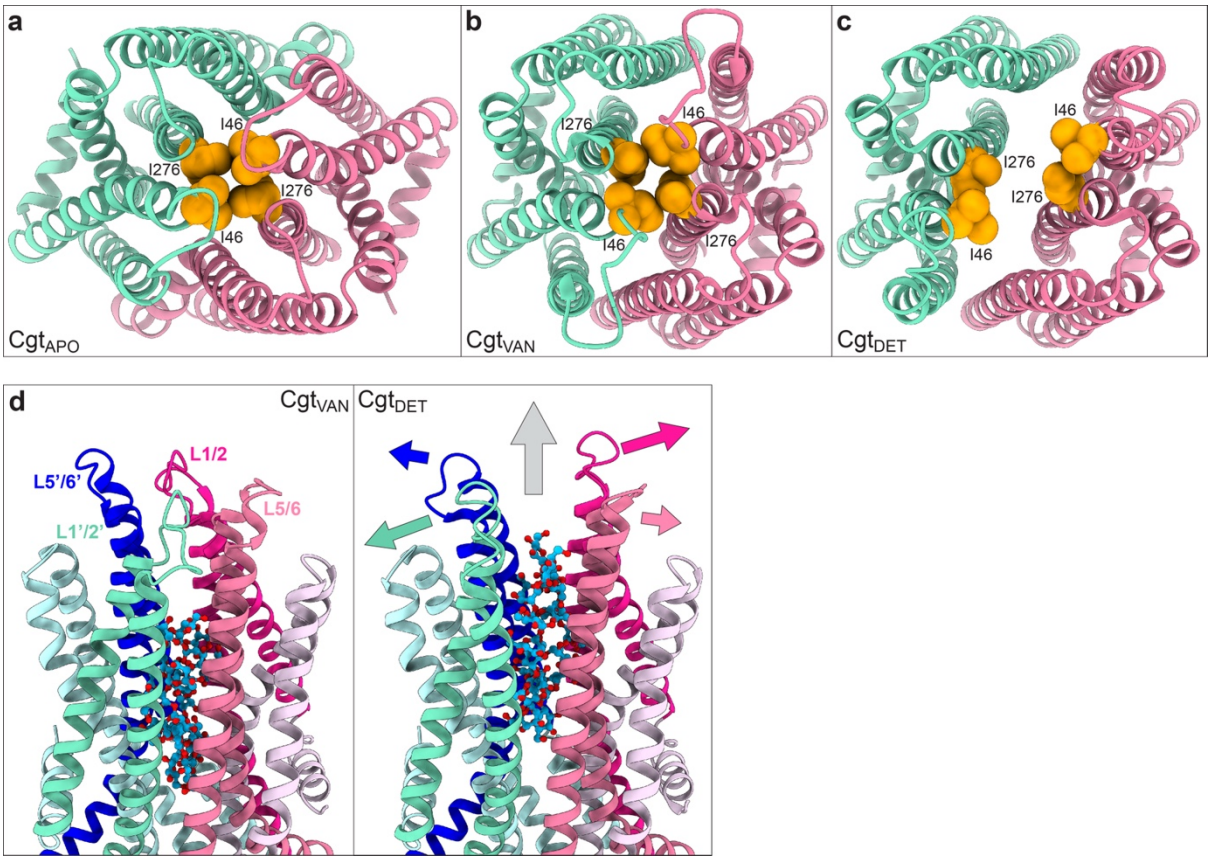

Extended Data Fig. 8 | Nucleotide-bound conformations of Cgt. a-c, Top view from the periplasmic side of Cgt highlighting the hydrophobic 'isoleucine gate' formed by residues I46 and I276. The gate is closed in the inward-facing state (Cgt_{APO}, a) as wells as in the closed-occluded conformation (Cgt_{VAN}, b). In the inward-facing Cgt_{DET} structure (c), the gate is open, allowing access from the central cavity to the periplasmic space. **d**, Periplasmic side of Cgt TM helices, indicating the proposed mechanism for opening of the central cavity to the outside. Chain A shown in purple and pink; chain B shown in blue and cyan. A CβG molecule (blue-red sticks) was docked into the central cavity. Rearrangements of TMs and periplasmic loops between the Cgt_{VAN} (left) and Cgt_{DET} (right) models are indicated with arrows. The resulting opening allows the release of the substrate into the periplasmic space (grey arrow).

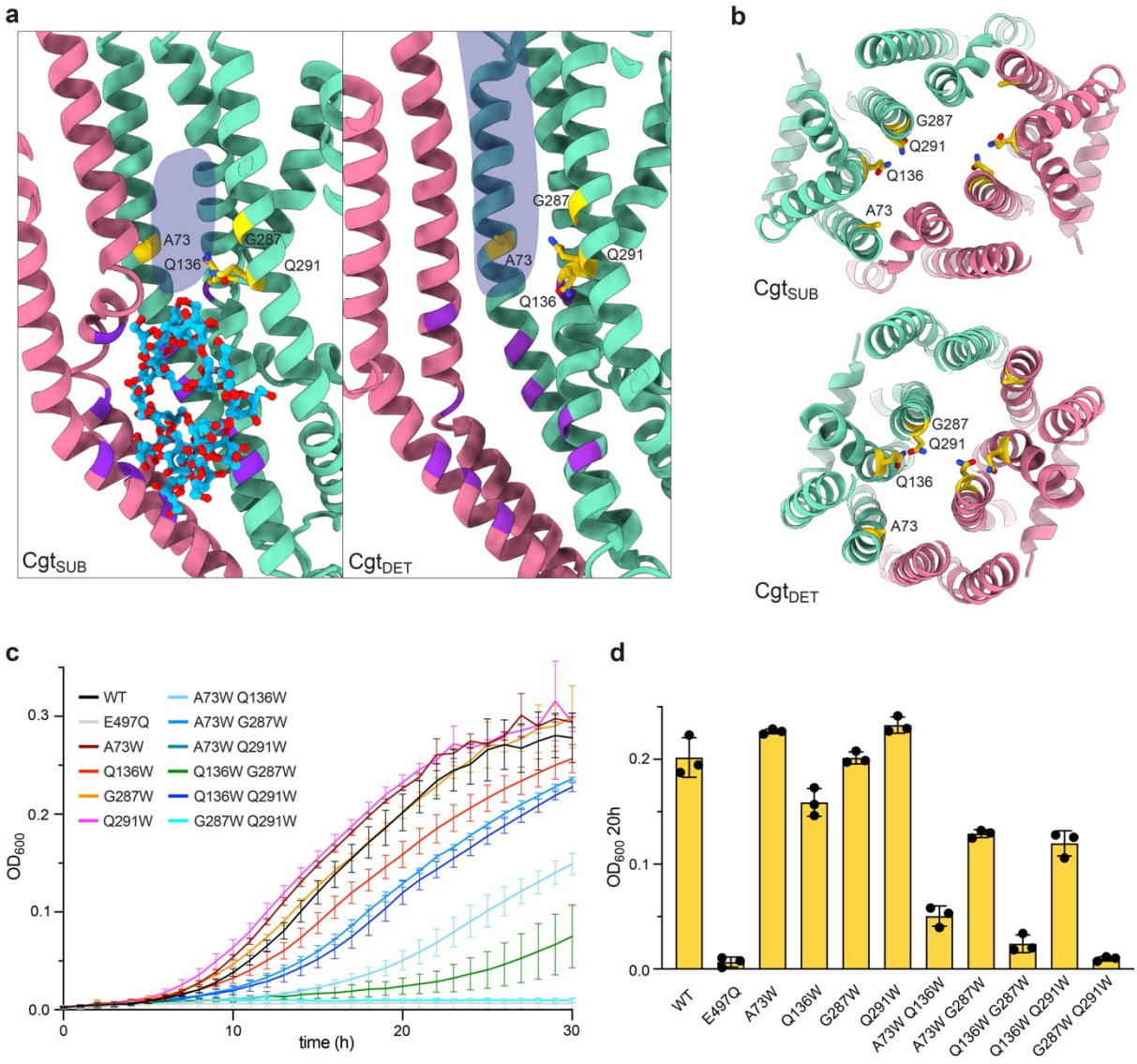

Extended Data Fig. 9 | Cgt substrate translocation. a, Side view of the central cavity of the Cgt$_{SUB}$ (left) and Cgt$_{DET}$ (right) models, indicating the CβG binding pocket residues (purple) and the free space in the central cavity (blue shading). Residues pointing towards the center of the inner cavity in both models that were targeted by Trp mutagenesis are shown in yellow. **b**, View of the inner part of the central cavity from the periplasmic space in Cgt$_{SUB}$ (top) and Cgt$_{DET}$ (bottom) models. Residues mutated to Trp are shown in yellow. **c, d**, In-vivo Cgt activity assay indicating the ability of different Trp mutants of Cgt to restore growth of *Atu Δcgt* under osmotic stress. Both growth curves (c) and a single 20h time point (d) are shown. Growth curves represent mean values of 3 independent experiments (n=3). Dots represent mean values of independent experiments (n=3). Error bars represent standard deviation. Data for graphs c-d are available as source data.

Data Availability

Atomic structure coordinates were deposited in the Protein Data Bank under accession codes PDB:7ZO8 (Cgt_{APO}), PDB:7ZOA (Cgt_{SUB}), PDB:7ZO9 (Cgt_{VAN}) and PDB:7ZNU (Cgt_{DET}). The cryo-EM maps were deposited in the Electron Microscopy Data Bank under accession codes EMD:14843 (Cgt_{APO}), EMD:14845 (Cgt_{SUB}). EMD:14844 (Cgt_{VAN}) and EMD:14814 (Cgt_{DET}).

Methods-only References

21. Thoma, S. and M. Schobert, *An improved Escherichia coli donor strain for diparental mating.* FEMS Microbiol Lett, 2009. **294**(2): p. 127-32.
22. Mastronarde, D.N., *Automated electron microscope tomography using robust prediction of specimen movements.* J Struct Biol, 2005. **152**(1): p. 36-51.
23. Zheng, S.Q., et al., *MotionCor2: anisotropic correction of beam-induced motion for improved cryo-electron microscopy.* Nat Methods, 2017. **14**(4): p. 331-332.
24. Biyani, N., et al., *Focus: The interface between data collection and data processing in cryo-EM.* J Struct Biol, 2017. **198**(2): p. 124-133.
25. Punjani, A., et al., *cryoSPARC: algorithms for rapid unsupervised cryo-EM structure determination.* Nat Methods, 2017. **14**(3): p. 290-296.
26. Rohou, A. and N. Grigorieff, *CTFFIND4: Fast and accurate defocus estimation from electron micrographs.* J Struct Biol, 2015. **192**(2): p. 216-21.
27. Waterhouse, A., et al., *SWISS-MODEL: homology modelling of protein structures and complexes.* Nucleic Acids Res, 2018. **46**(W1): p. W296-W303.
28. Kim, Y. and J. Chen, *Molecular structure of human P-glycoprotein in the ATP-bound, outward-facing conformation.* Science, 2018. **359**(6378): p. 915-919.
29. Pettersen, E.F., et al., *UCSF Chimera--a visualization system for exploratory research and analysis.* J Comput Chem, 2004. **25**(13): p. 1605-12.
30. Emsley, P., et al., *Features and development of Coot.* Acta Crystallogr D Biol Crystallogr, 2010. **66**(Pt 4): p. 486-501.
31. Afonine, P.V., et al., *Real-space refinement in PHENIX for cryo-EM and crystallography.* Acta Crystallogr D Struct Biol, 2018. **74**(Pt 6): p. 531-544.
32. Afonine, P.V., et al., *New tools for the analysis and validation of cryo-EM maps and atomic models.* Acta Crystallogr D Struct Biol, 2018. **74**(Pt 9): p. 814-840.
33. Williams, C.J., et al., *MolProbity: More and better reference data for improved all-atom structure validation.* Protein Sci, 2018. **27**(1): p. 293-315.